Supporting Information

Dual-site substitution enables high-voltage P2-$Na_{0.67}Ni_{0.33}Mn_{0.67}O_2$ cathodes with superior wide-temperature performance and enhanced ambient stability for sodium-ion batteries

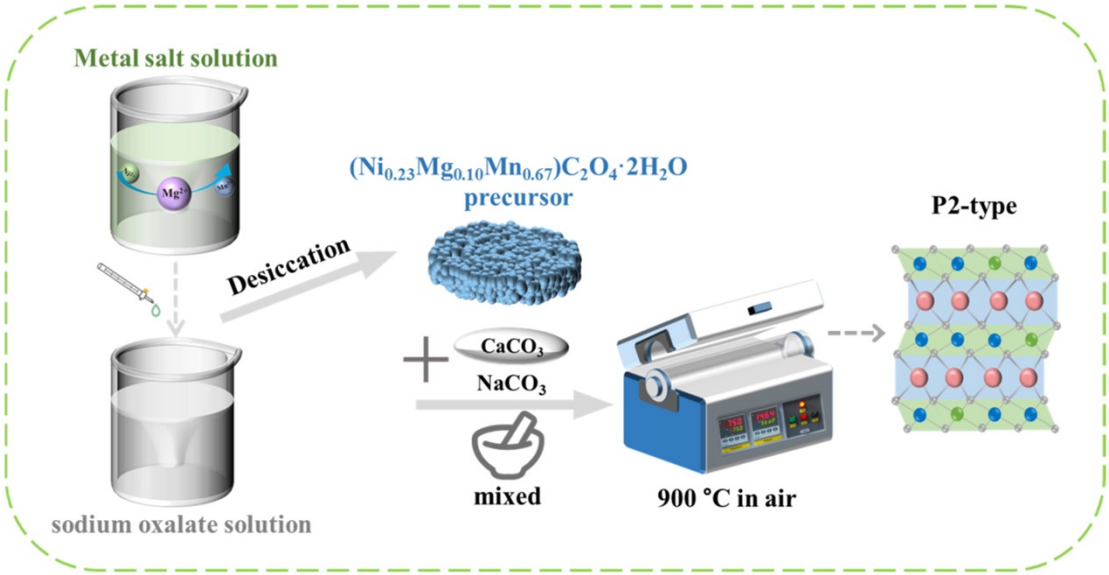

Figure S1. Schematic representation of Ca/Mg-doped cathode synthetic procedure.

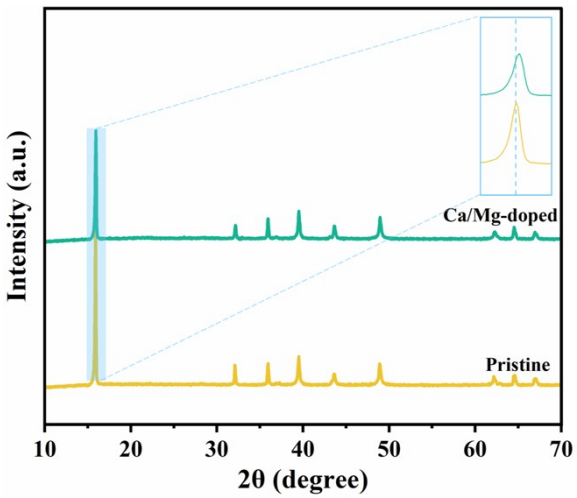

Figure S2. XRD patterns of Pristine and Ca/Mg doped cathodes.

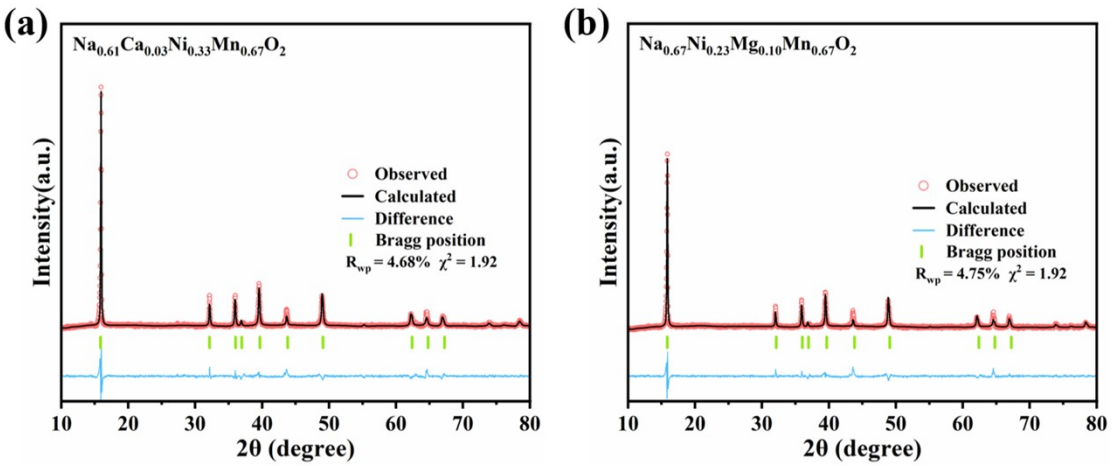

Figure S3. Rietveld refinement results of (a) Ca-doped and (b) Mg-doped samples.

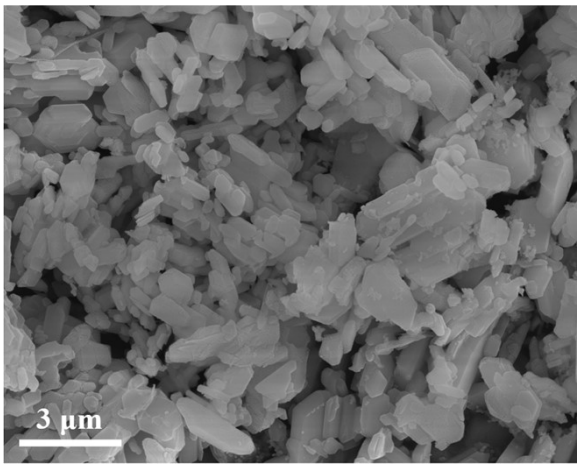

Figure S4. SEM image of the Pristine sample.

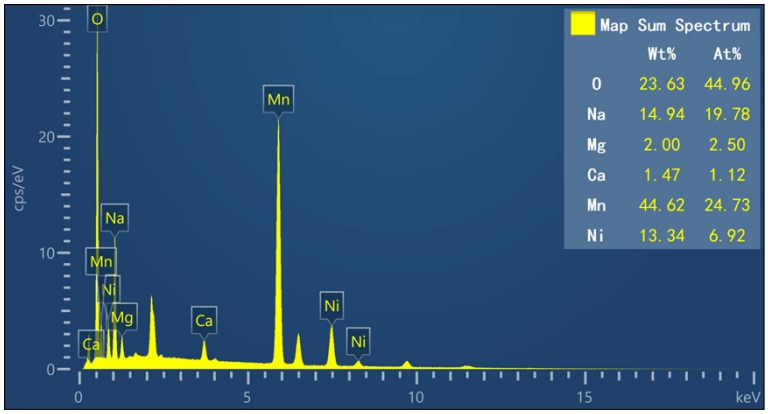

Figure S5. Elemental occupancy of the Ca/Mg-doped sample.

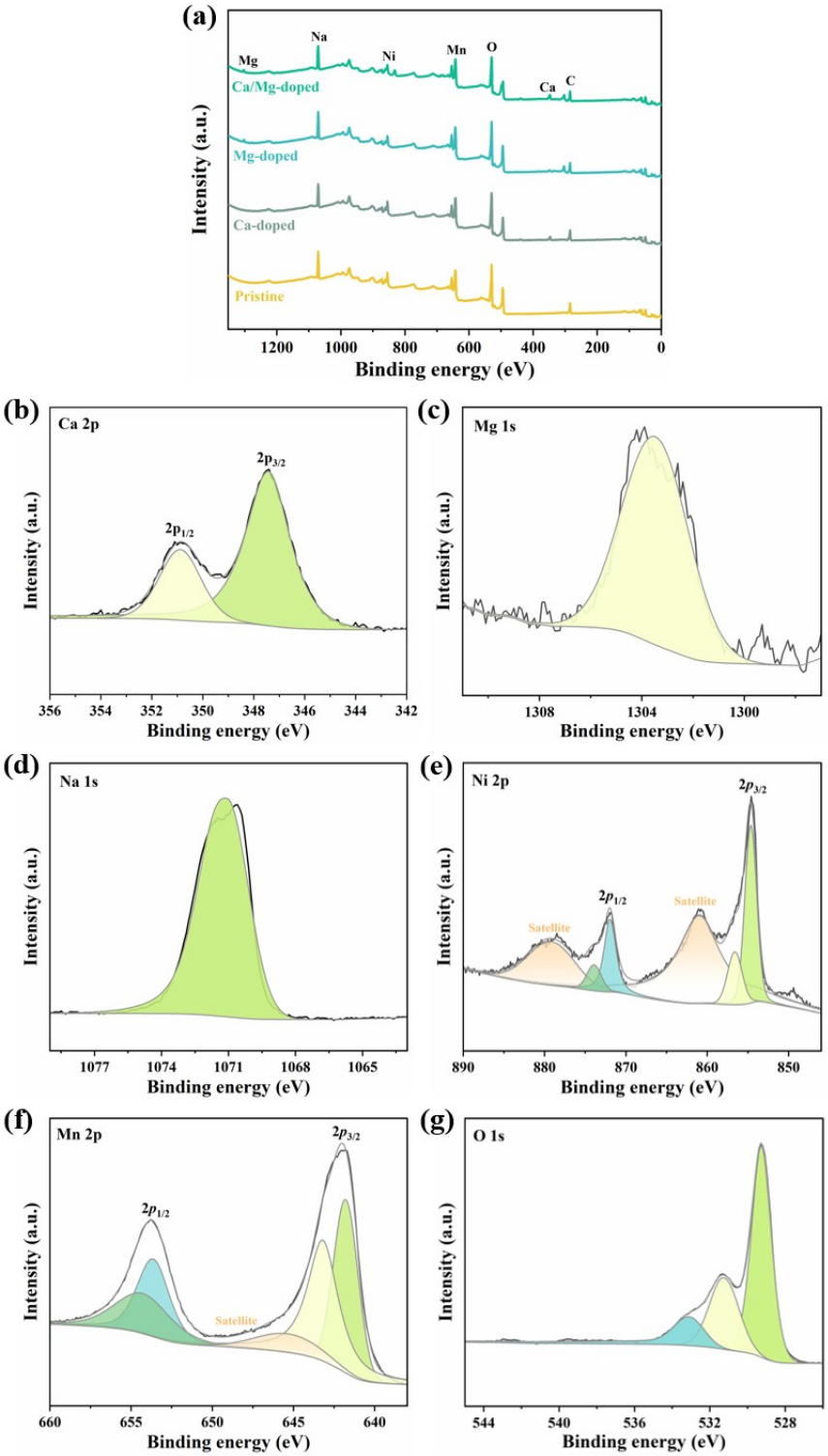

Figure S6. (a) The XPS full spectrum of all samples. XPS spectra of (b) Ca 2p, (c) Mg 1s, (d) Na 1s, (e) Ni 2p, (f) Mn 2p and (g) O 1s of Ca/Mg doped sample.

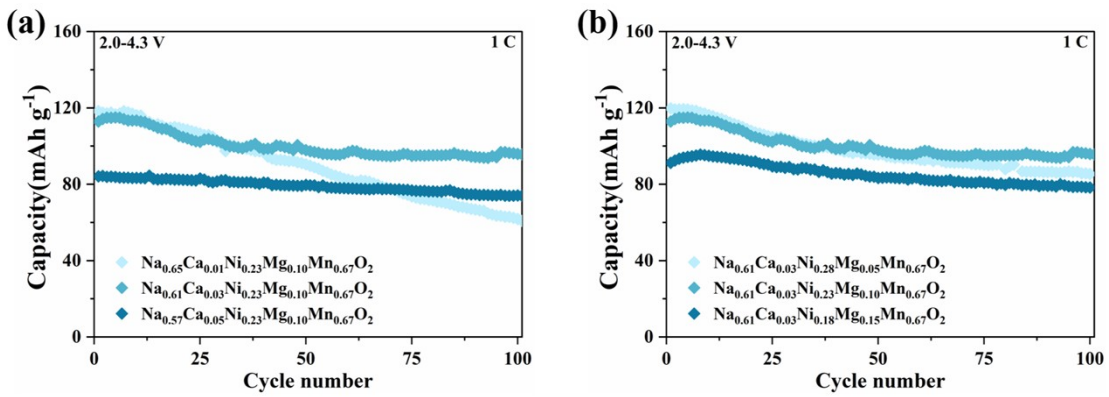

Figure S7. Cycling performance of $Na_{0.67}Ni_{0.33}Mn_{0.67}O_2$ with different doping amounts of Ca^{2+} and Mg^{2+} at 1 C.

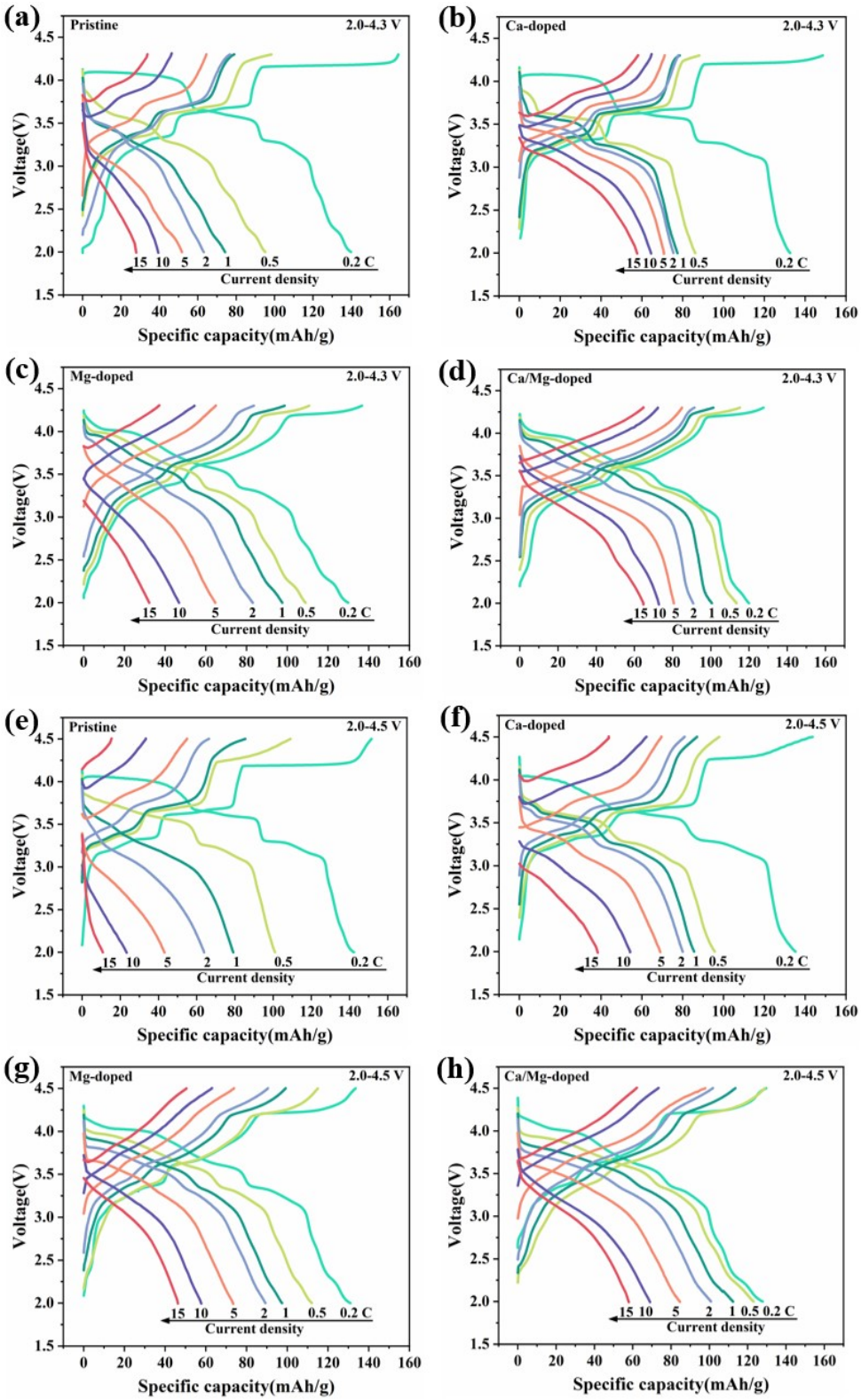

Figure S8. Rate capabilities of (a, e) Pristine, (b, f) Ca-doped, (c, g) Mg-doped and (d, h) Ca/Mg-doped cathodes within 2.0-4.3 V and 2.0-4.5 V, respectively.

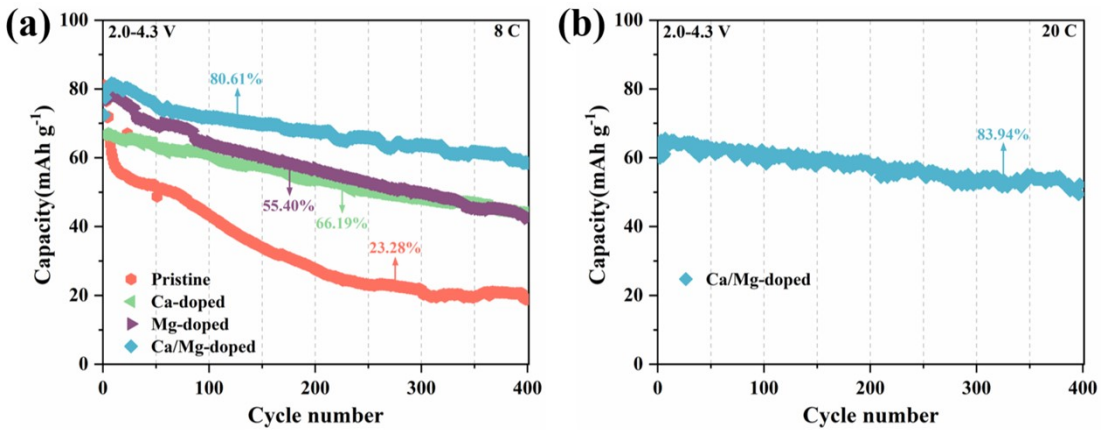

Figure S9. (a) long-term cycling stability of the synthesized samples tested at 8 C and (b) Long-term cycling of Ca/Mg-doped cathode at 20 C .

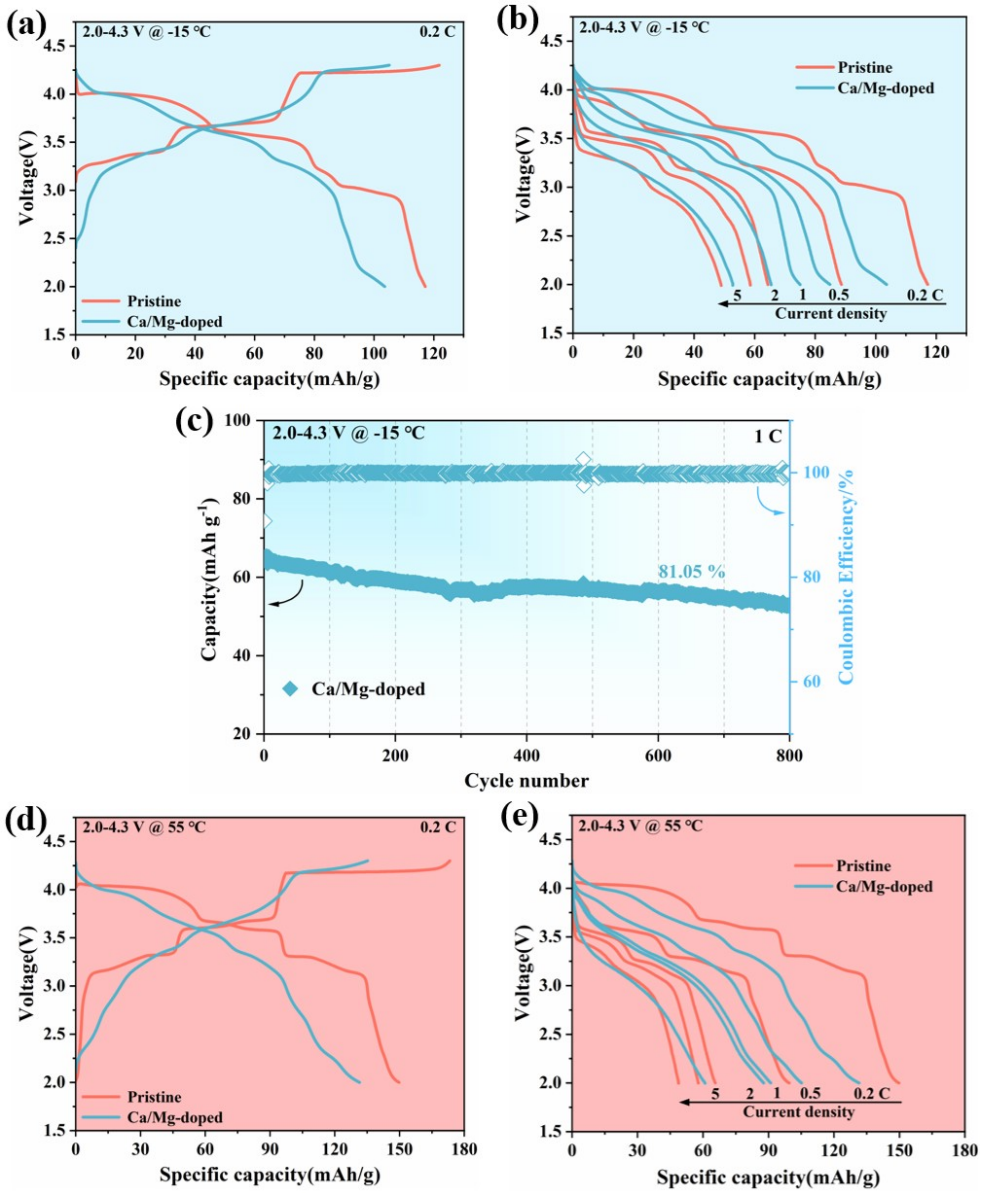

Figure S10. Low-temperature (-15 °C) performance with (a) charge-discharge profiles and (b) rate retention, and (c) cycling stability of Ca/Mg-doped cathodes over 800 cycles at 1 C. High-temperature (55 °C) performance with (d) charge-discharge profiles and (e) rate retention at 1 C.

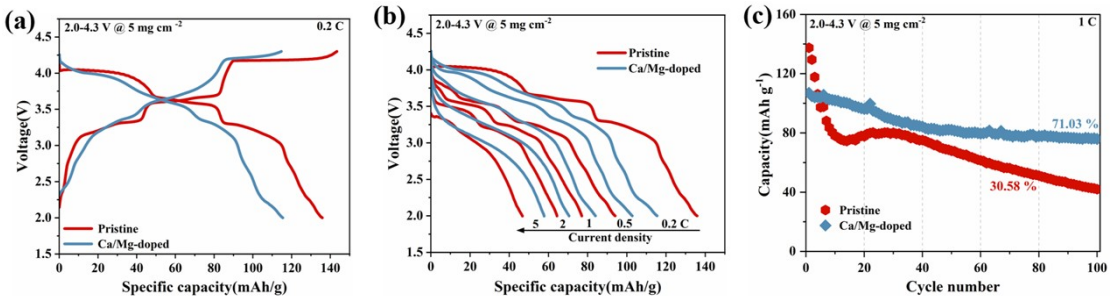

Figure S11. Electrochemical performance under high mass loading (5 mg cm^{-2}): (a) initial charge/discharge profiles, (b) rate capability, and (c) cycling stability.

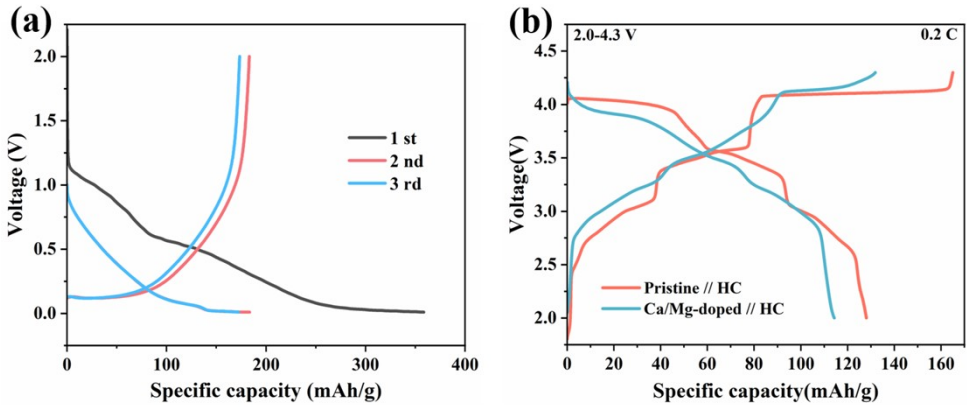

Figure S12. (a) The hard carbon half-cell at a current of 0.1A g^{-1} in the voltage range of 0.01-2.0 V. (b) Full-cell performance: Initial galvanostatic charge-discharge profiles at 0.2 C.

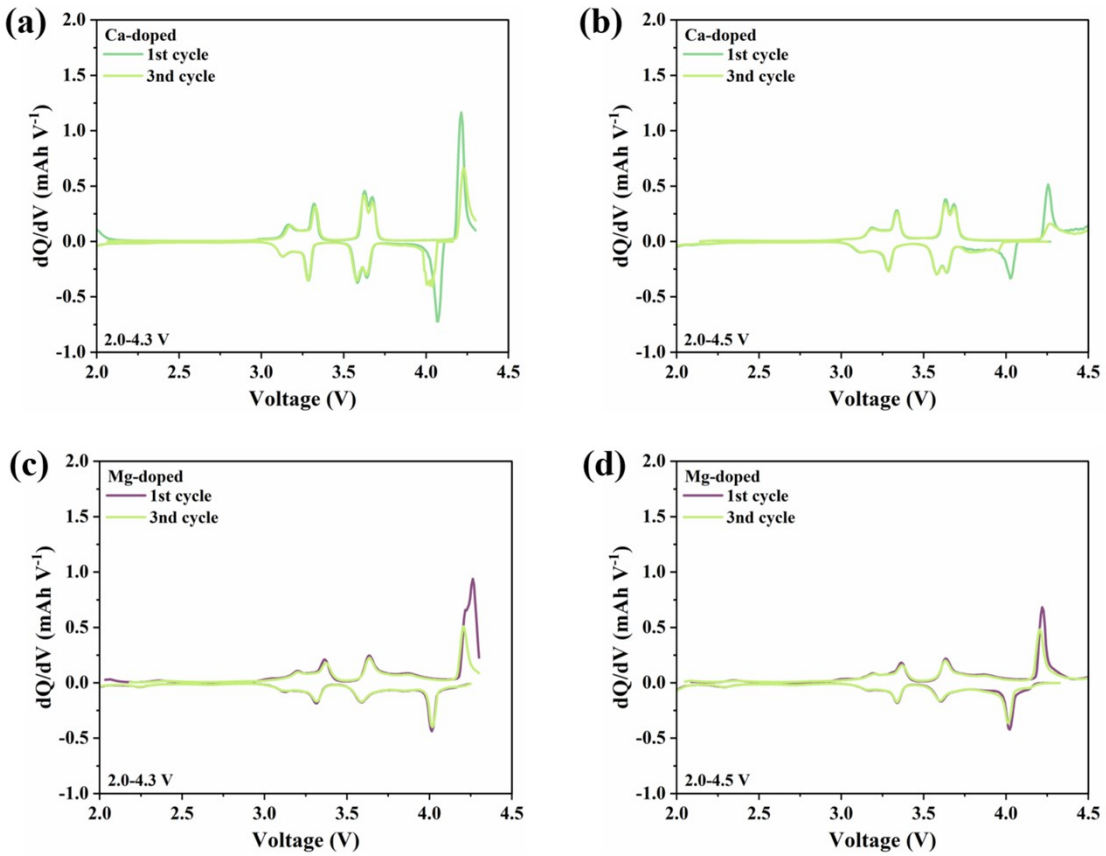

Figure S13. The dQ/dV plots for as-prepared Ca-doped within 2.0-4.3V (a) and 2.0-4.5V (b), and Mg-doped cathodes within (c) 2.0-4.3 V and (d) 2.0-4.5 V voltage.

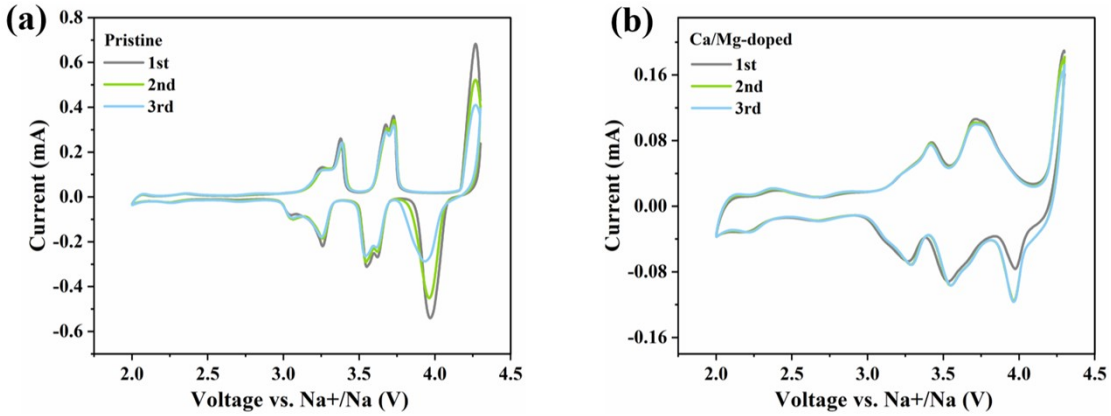

Figure S14. CV curves of (a) Pristine and (b) Ca/Mg-doped at 0.1 mV s^{-1}.

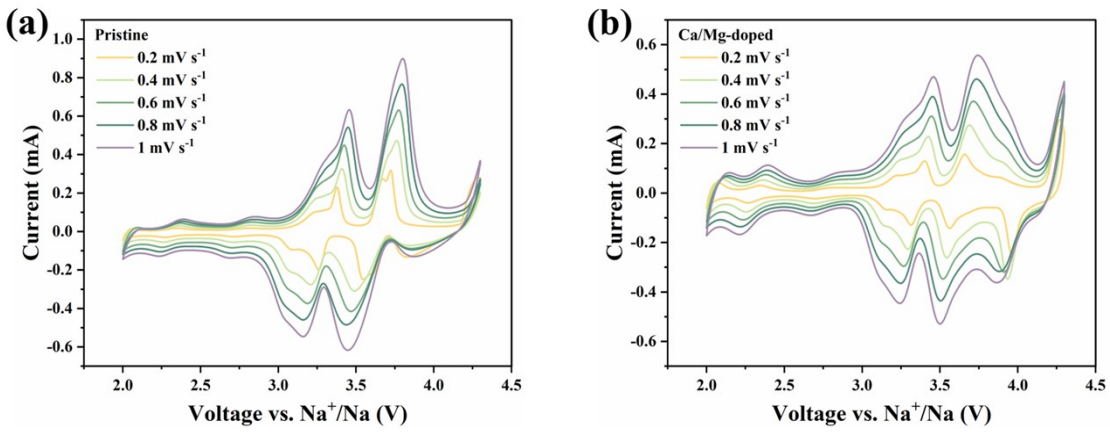

Figure S15. CV curves of the (a) Pristine and (b) Ca/Mg-doped electrode at different scan rates ranging from 0.2 to 1.0 mV s^{-1}.

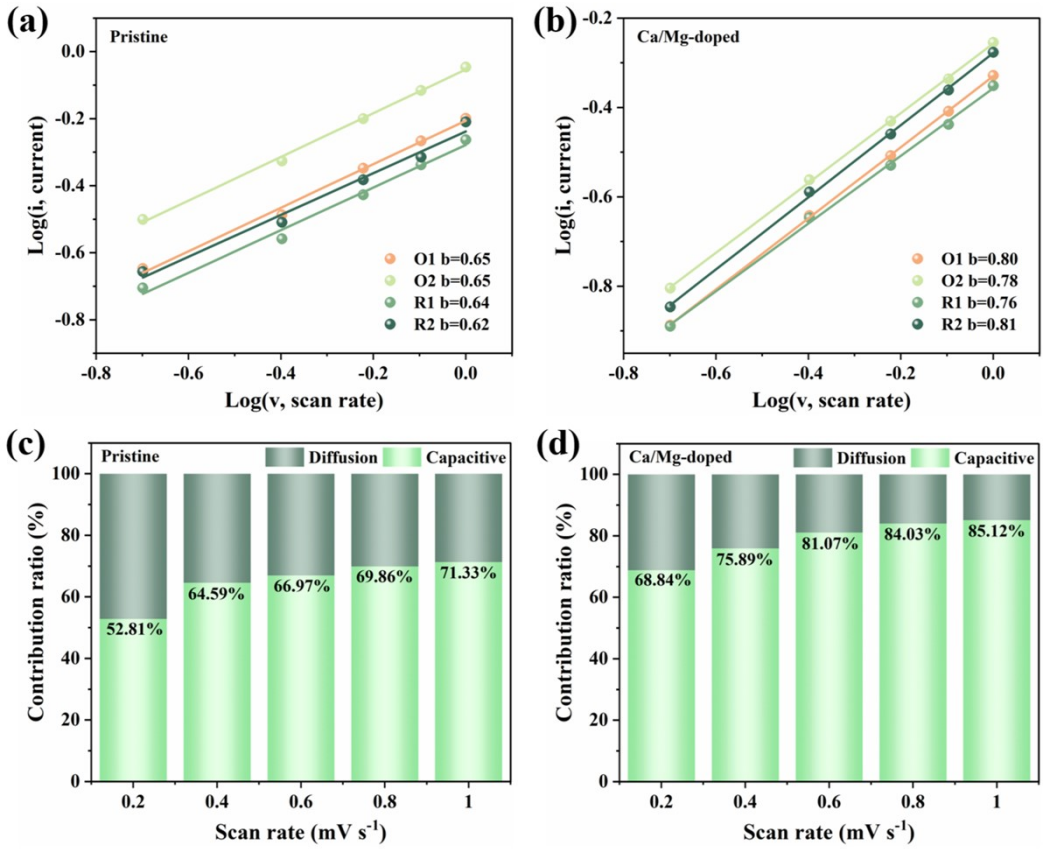

Figure S16. (a, b) Linear relationship of peak currents log(i) versus log(v) and the corresponding linear fits. (c, d) Contribution ratio of capacitive and diffusion-controlled behaviors at different scan rates.

The b-value is utilized to assess the charge storage mechanism in cathode materials, distinguishing between faradaic intercalation and surface-controlled capacitive behavior. Based on the power-law relationship between peak current (i) and scan rate (v), Eq. S1 be expressed as follows[S1]:

$$i = av^b \qquad \text{Eq.(S1)}$$

The capacitive contribution ratio can be determined through the functional relationship between current (i) and voltage (V), as defined by Eq. S2:

$$i(V) = k_1 v + k_2 v^{1/2} \qquad \text{Eq.(S2)}$$

Where k_1 and k_2 are the calculated coefficients at that voltage. k_1v quantifies the contribution of pseudocapacitance at voltage.

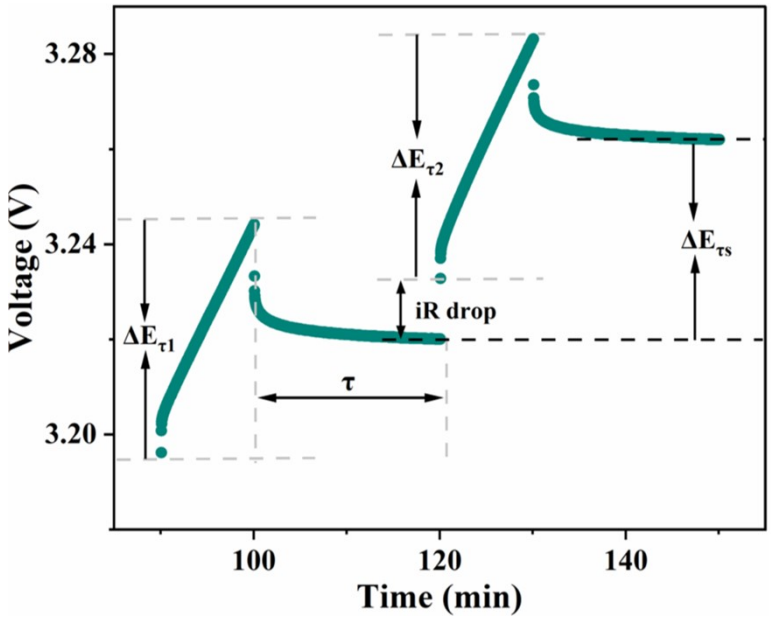

Figure S17. Illustration of the relationship of ΔEs, ΔEτ, and τ in the sodium-ion diffusion coefficient (D_{Na+}) calculation formula.

Galvanostatic intermittent titration technique (GITT) measurements were conducted during the second cycle to determine the sodium ion diffusion coefficient (D_{Na+}) in the prepared cathodes. The D_{Na+} values were calculated using the following equation:

$$D_{Na+} = \frac{4}{\pi\tau}\left(\frac{mBVm}{MBS}\right)^2\left(\frac{\Delta Es}{\Delta E\tau}\right)^2 \qquad \text{Eq.(S3)}$$

where τ represents the galvanostatic current pulse duration, m_B, V_M, and M_B, denote the active material mass, molar volume, and the molecular weight of the NFM sample, respectively; S is the electrode-electrolyte contact surface area, while ΔE_s and ΔE_τ correspond to the steady-state voltage shift and the voltage variation during the pulse, respectively[S2].

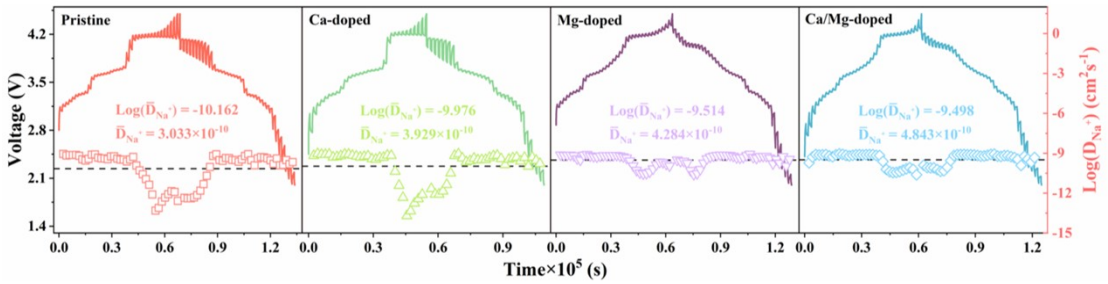

Figure S18. GITT measurements and corresponding Na^+ diffusion coefficients at 2.0-4.5 V.

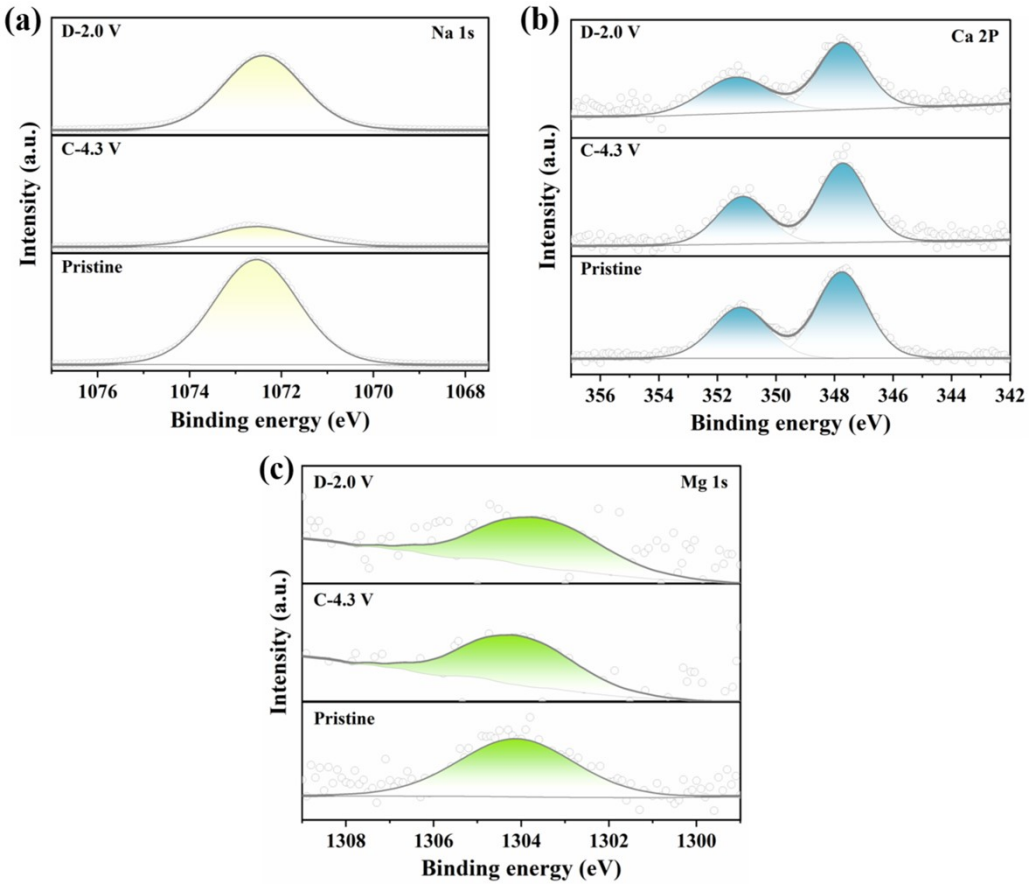

Figure S19. XPS spectra of (a) Na1s, (b) Ca 2p, and (c) Mg 1s in Ca/Mg-doped during the initial cycle.

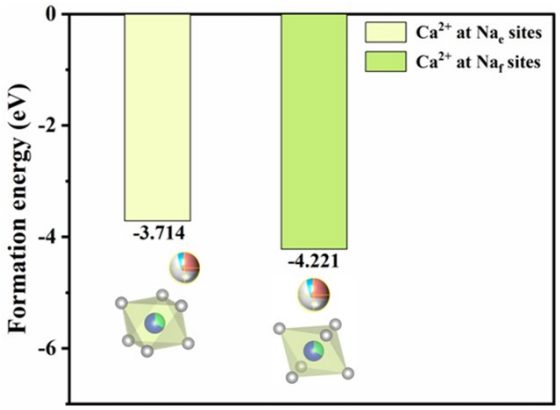

Figure S20. Formation energy comparison of Ca^{2+} at Na_e and Na_f sites.

Computational details

All the calculations are performed in the framework of the density functional theory with the projector augmented plane-wave method, as implemented in the Vienna ab initio simulation package[S3]. The generalzied gradient approximation proposed by Perdew, Burke, and Ernzerhof is selected for the exchange-correlation potential[S4]. The long range van der Waals interaction is described by the DFT-D3 approach[S5]. The cut-off energy for plane wave is set to 500 eV. The energy criterion is set to 10-5 eV in iterative solution of the Kohn-Sham equation. The Brillouin zone integration is performed using a 3×3×1 k-mesh. All the structures are relaxed until the residual forces on the atoms have declined to less than 0.03 eV/Å. Employing the climbing image nudged elastic band method (CI-NEB), we computed the minimum energy pathway of the cyclization reaction along with its corresponding activation barrier.

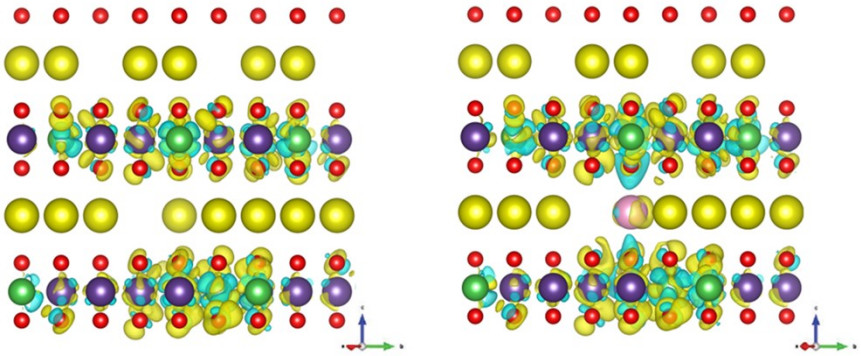

Figure S21. 3D Charge density difference maps for Pristine and Ca/Mg-doped structures.

Table S1. The calculated formation energy of Ca^{2+} or Mg^{2+} at Na or TM sites in $Na_{0.67}Ni_{0.33}Mn_{0.67}O_2$, unit: eV

	E(doped)	E(NNMO)	E(TM)	E(Na)	E(Ca or Mg)	ΔE(formation)
Ca-doped in Na	-442.623	-439.903	-5.885	-1.471	-2.168	-2.024
Ca-doped in TM	-439.019	-439.903				-2.833
Mg-doped in Na	-441.156	-439.903			-1.799	-0.926
Mg-doped in TM	-439.713	-439.903				-3.897

The formation energy of Ca or Mg at Na or TM site in $Na_{0.67}Ni_{0.33}Mn_{0.67}O_2$ is calculated by the following equation:

$$\Delta E\ (\text{formation}) = E\ (\text{doped}) + E\ (\text{Na}) - E\ (\text{NNMO}) - E\ (\text{Ca or Mg}) \quad \text{Eq.(S4)}$$

$$\Delta E\ (\text{formation}) = E\ (\text{doped}) + E\ (\text{TM}) - E\ (\text{NNMO}) - E\ (\text{Ca or Mg}) \quad \text{Eq.(S5)}$$

where E (doped) represents the energy of $Na_{0.67}Ni_{0.33}Mn_{0.67}O_2$ with Ca or Mg doped at Na or TM sites, E(NNMO) is the energy of the of the original $Na_{0.67}Ni_{0.33}Mn_{0.67}O_2$, and E (Na), E (Ca or Mg), E (TM) are the chemical potential of Na, Ca or Mg and the transition metal, respectively.

Discussion on the site preference of Ca^{2+} and Mg^{2+} in P2-$Na_{0.67}Ni_{0.33}Mn_{0.67}O_2$

DFT calculations were performed to evaluate the formation energy of Ca and Mg at both Na and TM sites, as summarized in Table S1. The results reveal a pronounced thermodynamic driving force for Mg to occupy the TM layer, with formation energies of -0.926 eV at the Na site and -3.897 eV at the TM site. This strong preference is fully consistent with the experimental observation.

For Ca, the calculated formation energy at the TM site (-2.833 eV) is slightly lower than that at the Na site (-2.024 eV), indicating a marginal thermodynamic preference for TM occupation under idealized equilibrium conditions. However, site occupancy during solid-state synthesis can also be influenced by kinetic factors, which may become relevant under the specific conditions employed in this work. Specifically, the two-step synthesis protocol involves pre-forming a (Ni, Mg, Mn)-oxalate precursor that establishes the TM-layer framework with Mg already incorporated. Only during the subsequent high-temperature calcination are Na_2CO_3 and $CaCO_3$ introduced simultaneously. At this stage, Ca^{2+} encounters a substantial kinetic barrier to diffuse

into the pre-constructed, densely packed TM-O slabs, whereas the Na layer—already designed with reduced Na occupancy (Na content intentionally decreased from 0.67 to 0.61 to accommodate 0.03 Ca^{2+})—provides readily accessible vacancies. Given the calculated thermodynamic preference and the constraints of the two-step synthetic route, it is reasonable to infer that kinetic factors during the non-equilibrium calcination process favor Ca occupancy in the Na layer over the TM layer. This interpretation aligns with the crystallographic evidence from Rietveld refinement (Table S3), which shows an expansion of the Na-layer spacing upon Ca doping and a contraction of the TM layer driven by Mg substitution.

Table S2. Designed compositions of four synthesized samples.

Designed Composition of Sample	Abbreviations	Doping Ca atom %	Doping Mg atom %
$Na_{0.67}Ni_{0.33}Mn_{0.67}O_2$	Pristine	0	0
$Na_{0.61}Ca_{0.03}Ni_{0.33}Mn_{0.67}O_2$	Ca-doped	3	0
$Na_{0.67}Ni_{0.23}Mg_{0.10}Mn_{0.67}O_2$	Mg-doped	0	10
$Na_{0.61}Ca_{0.03}Ni_{0.23}Mg_{0.10}Mn_{0.67}O_2$	Ca/Mg-doped	3	10

Table S3. Results of XRD Rietveld refinement for Pristine, Ca-doped, Mg-doped and Ca/Mg-doped cathodes.

	Pristine	Ca-doped	Mg-doped	Ca/Mg-doped
R_{wp} (%)	4.506	4.682	4.750	4.742
χ^2	1.84	1.96	1.92	1.88
a (Å)	2.88735	2.89530	2.88521	2.88649
b (Å)	2.88735	2.89530	2.88521	2.88649
c (Å)	11.17090	11.18100	11.17460	11.14334
V ($Å^3$)	80.652475	81.170530	80.559632	80.405286
Na layer (Å)	3.4742(4)	4.08(3)	3.8336(4)	3.6307(4)
TM layer (Å)	2.11132(7)	1.51	1.7537(2)	1.9409(7)

Table S4. ICP-OES results of as-prepared samples.

Theoretical chemical formula	Measured atomic ratio				
	Na	Ca	Ni	Mg	Mn
$Na_{0.61}Ca_{0.03}Ni_{0.23}Mg_{0.10}Mn_{0.67}O_2$	0.584	0.028	0.244	0.092	0.664

Table S5. The Ni^{2+}/ Ni^{3+}ratio based on XPS results of all synthesized samples.

Pristine ($\sum\chi^2$=9.05)		BE (eV)	Content (%)	Ration of Ni^{2+}/ Ni^{3+}
Ni^{2+}	Ni $2p_{3/2}$	854.41	58.18	1.39
	Ni $2p_{1/2}$	871.83		
Ni^{3+}	Ni $2p_{3/2}$	855.64	41.82	
	Ni $2p_{1/2}$	873.25		

Ca-doped ($\sum\chi^2$=7.95)		BE (eV)	Content (%)	Ration of Ni^{2+}/ Ni^{3+}
Ni^{2+}	Ni $2p_{3/2}$	854.45	60.27	1.52
	Ni $2p_{1/2}$	871.87		
Ni^{3+}	Ni $2p_{3/2}$	855.90	39.73	
	Ni $2p_{1/2}$	873.34		

Mg-doped ($\sum\chi^2$=6.93)		BE (eV)	Content (%)	Ration of Ni^{2+}/ Ni^{3+}
Ni^{2+}	Ni $2p_{3/2}$	854.44	69.96	2.33
	Ni $2p_{1/2}$	871.74		
Ni^{3+}	Ni $2p_{3/2}$	855.99	30.04	
	Ni $2p_{1/2}$	873.29		

Ca/Mg-doped ($\sum\chi^2$=8.76)		BE (eV)	Content (%)	Ration of Ni^{2+}/ Ni^{3+}
Ni^{2+}	Ni $2p_{3/2}$	854.66	74.08	2.86
	Ni $2p_{1/2}$	871.96		
Ni^{3+}	Ni $2p_{3/2}$	856.61	25.92	
	Ni $2p_{1/2}$	873.91		

Table S6. Comparison of half-cell electrochemical performance between the Ca/Mg-doped cathode and other reported layered transition metal oxide cathodes.

Samples	Current rate ($mA\ g^{-1}$)	Retention (%) (no. of cycles)	Ref.
$Na_{0.7}Li_{0.03}Mg_{0.03}Ni_{0.27}Mn_{0.6}Ti_{0.07}O_2$	346	82 (200th)	[S6]
$Na_{0.80}Mg_{0.03}Li_{0.18}Mn_{0.67}Cu_{0.15}O_2$	1000	80.3 (300th)	[S7]
$Na_{0.66}Ni_{0.27}Zn_{0.06}Mn_{0.61}Ti_{0.06}O_2$	500	76.01 (500th)	[S8]
$Na_{0.637}B_{0.038}MnO_2$	160	81 (100th)	[S9]
$Na_{0.6}Ni_{0.25}Al_{0.1}Mn_{0.65}O_2$	170	64.36 (100th)	[S10]
Li_2TiO_3@$Na_{0.67}Mn_{0.5}Fe_{0.5}O_2$	17	63.3 (50th)	[S11]
$Na_{0.75}[Li_{0.15}Ni_{0.15}Mn_{0.7}]O_2$	26	73 (300th)	[S12]
$Na_{0.55}[Ni_{0.1}Fe_{0.1}Mn_{0.8}]O_2$	60	75 (100th)	[S13]
$Na_{0.696}Ni_{0.329}Mn_{0.671}O_2$	170	71.9 (1000th)	[S14]
Ca/Mg-doped	100	82.32 (200th)	This work
	800	80.61 (400th)	
	2000	83.94 (400th)	

Table S7. Comparison of electrochemical performance between the Ca/Mg-doped cathode and other reported cathode materials for sodium-ion batteries.

Material type	Samples	Voltage window	Initial capacity (mAh g^{-1})	Retention (%)	Rate capability (mAh g^{-1})	Ref.
Typical P2-type oxides	$Na_{0.61}Ca_{0.03}Ni_{0.23}Mg_{0.10}Mn_{0.67}O_2$	2.0-4.3V 2.0-4.5V	112.81(1C)	82.3(200th,2.0-4.3V) 73.3(200th,2.0-4.5V)	72.8(10C) 64.6(15C)	This work
	$Na_{0.66}Li_{0.18}Fe_{0.12}Mn_{0.7}O_2$	1.5-4.5V	214(0.05C)	86.8(80th,1.5-4.5V)	141.1(1C)	S15
	$Na_{0.67}Zn_{0.05}Ni_{0.15}Fe_{0.2}Mn_{0.6}O_{1.95}F_{0.05}$	2.0-4.1V 1.5-4.3V	116(1C)	80.1(200th,2.0-4.1V) 67(100th,1.5-4.3V)	62(10C)	S16
NASICON-type	$Na_4Fe_{2.85}Mg_{0.15}(PO_4)_2P_2O_7$	1.5-4.0V	103.8(0.2C)	93.6(450th,1.5-4.0V)	41.6(10C)	S17
	$Na_4(Mn_{0.5}Fe_{0.5})_{2.94}Nb_{0.06}(PO_4)_2P_2O_7$	1.7-4.3V	90.2(1C)	90.3(300th,1.7-4.3V)	71.3(10C)	S18
	$Na_{2.9}MnTi_{0.95}Mo_{0.05}(PO_4)_3$	2.5-4.2V	94(0.5C)	78.7(600th,2.5-4.2V)	70(5C)	S19
Prussian blue analogue materials	$Na_2Ti_{0.5}V_{0.5}[Fe(CN)_6]$	2.0-4.5V	68.7(0.1C)	90.8(200th,2.0-4.5V)	59(10C)	S20
	$Na_{1.59}Fe[Fe(CN)_6]_{0.95}\cdot 2.8H_2O$	2.0-3.8V 2.0-4.0V	100(1C)	98.2(300th,2.0-3.8V) 73.4(200th,2.0-4.0V)	85.2(5C)	S21
	$Na_{1.27}Fe[Fe(CN)_6]\cdot 1.26H_2O$	2.0-4.0V	85.5(20C)	70(10000th,2.0-4.0V)	51(100C)	S22

Our material is strategically designed to achieve a balanced trade-off between specific capacity and overall electrochemical performance. Although its specific capacity is lower than that of conventional P2-type oxides, it is capable of operating at a higher cut-off voltage, which provides enhanced structural stability, high-voltage compatibility, excellent ambient stability, and wide-temperature applicability.

NASICON-type materials typically operate below 4.0 V, suffer from intrinsically poor electronic conductivity that necessitates supplemental carbon coating, and deliver only modest rate capability. In contrast, our material sustains reliable high-voltage operation up to 4.5 V with a capacity retention of 73.25 % after 200 cycles and exhibits superior rate performance of 72.8 mAh g^{-1} at 10 C, all without requiring complex carbon coating procedures. Prussian blue analogues (PBAs) experience severe capacity degradation when the upper cut-off voltage exceeds 4.0 V, often compelling operation within a restricted voltage window to preserve cycling stability, and they additionally raise safety and environmental concerns owing to the presence of toxic cyanide groups. Relative to PBAs, our material maintains stable cycling at 4.5 V, eliminates toxicity issues, and benefits from a simpler synthesis route. Beyond electrochemical considerations, our material possesses a high compaction density of 3.16 g cm^{-3}, which substantially exceeds the typical ranges observed for NASICON (1.0-1.8 g cm^{-3}) [S23]and PBA (0.7-1.6 g cm^{-3}) [S24] materials. This high compaction density directly contributes to superior volumetric energy density. Furthermore, our material exhibits ambient stability and is prepared via a straightforward calcination process that avoids both carbon coating and the handling of toxic precursors. Collectively, these attributes establish our material as a high-voltage, wide-temperature cathode that effectively balances energy density, rate capability, cycling stability, manufacturability, safety, and environmental robustness, thereby occupying a distinct niche for applications that demand reliable performance under challenging operating conditions.

Table S8. Comparison of the low- and high-temperature electrochemical performance between Ca/Mg-doped cathode with other reported layered oxides cathodes.

Samples	Low temperature Capacity retention	Room temperature Capacity retention	High temperature Capacity retention
$Na_{0.61}Ca_{0.03}Ni_{0.23}Mg_{0.10}Mn_{0.67}O_2$ (This work)	90.7 %@1 C 200 cycles 81 %@1 C 800 cycles (2.0-4.3 V) -15 ℃	82.3 %@1 C 200 cycles (2.0-4.3 V) 73.3 %@1 C 200 cycles (2.0-4.5 V)	65.7 %@1 C 150 cycles (2.0-4.3 V) 55 ℃
$Na_{0.76}Ni_{0.225}Mg_{0.025}Mn_{0.75}O_{1.95}F_{0.05}$ [S25]	95 %@100 mA g^{-1} 150 cycles (2.0-4.3 V) 0 ℃	83 %@100 mA g^{-1} 150 cycles (2.0-4.3 V)	52 %@100 mA g^{-1} 150 cycles (2.0-4.3 V) 55 ℃
$Na_{0.696}Ni_{0.329}Mn_{0.671}O_2$ [S26]	95.2 %@170 mA g^{-1} 100 cycles (2.0-4.13 V) -30 ℃	71.9 %@170 mA g^{-1} 1000 cycles (2.0-4.13 V)	65 %@170 mA g^{-1} 1000 cycles (2.0-4.13 V) 60 ℃
NaCrO2 [S27]	97.2 %@120 mA g^{-1} 100 cycles (2.9-3.3 V) -20 ℃	59 %@1200 mA g^{-1} 1000 cycles (2.9-3.3 V)	—
$Na_{2/3}Ni_{1/4}Cu_{1/12}Mn_{2/3}O_2$ [S28]	95.4 %@100 mA g^{-1} 500 cycles (1.5-3.65 V) -40 ℃	86.2 %@100 mA g^{-1} 500 cycles (1.5-3.65 V)	—
$Na_{0.67}Ni_{0.1}Co_{0.1}Mn_{0.8}O_2$ [S29]	80 %@1 C 300 cycles (1.5-4.2 V) -20 ℃	82.3 %@2 C 200 cycles (1.5-4.2 V)	—

Table S9. Results of XRD Rietveld refinement for Pristine, and Ca/Mg-doped cathodes after 50 cycles at 1 C.

	Pristine	Ca/Mg-doped
R_{wp} (%)	4.506	4.742
χ^2	1.84	1.88
a (Å)	2.88010	2.88037
b (Å)	2.88010	2.88037
c (Å)	11.14100	11.16910

References

[S1] Zhang J, Lai Y Y, Li P, et al. "Boosting rate and cycling performance of K-doped $Na_3V_2(PO_4)_2F_3$ cathode for high-energy-density sodium-ion batteries." *Green Energy & Environment* 7.6 (2022): 1253-1262. https://doi.org/10.1016/j.gee.2020.09.011.

[S2] Guo S, Peng J, Sharma N, et al. "Optimizing Sc-Doped $Na_3V_2(PO_4)_2F_3$/C as a High-Performance Cathode Material for Sodium-Ion Battery Applications." *Chemistry of Materials* 37.4 (2025): 1500-1512. https://doi.org/10.1021/acs.chemmater.4c02872

[S3] Kresse G, Joubert D. "From ultrasoft pseudopotentials to the projector augmented-wave method." *Physical review b* 59.3 (1999): 1758. https://doi.org/10.1103/PhysRevB.59.1758

[S4] Perdew J P, Burke K, Ernzerhof M. "Generalized gradient approximation made simple." *Physical review letters* 77.18 (1996): 3865. https://doi.org/10.1103/PhysRevLett.77.3865

[S5] Grimme S, Antony J, Ehrlich S, et al. "A consistent and accurate ab initio parametrization of density functional dispersion correction (DFT-D) for the 94 elements H-Pu." *The Journal of chemical physics* 132.15 (2010). https://doi.org/10.1063/1.3382344

[S6] Cheng Z, Zhao B, Guo Y J, et al. "Mitigating the large-volume phase transition of P2-type cathodes by synergetic effect of multiple ions for improved sodium-ion batteries." *Advanced Energy Materials* 12.14 (2022): 2103461. https://doi.org/10.1002/aenm.202103461

[S7] Xiao J, Gao H, Xiao Y, et al. "A hydro-stable and phase-transition-free P2-type cathode with superior cycling stability for high-voltage sodium-ion batteries." *Chemical Engineering Journal* 506 (2025): 160010. https://doi.org/10.1016/j.cej.2025.160010

[S8] Huang J, Xu L, Ye D, et al. "Suppressing the P2–O2 phase transition of P2-type Ni/Mn-based layered oxide by synergistic effect of Zn/Ti co-doping for advanced sodium-ion batteries." *Journal of Alloys and Compounds* 976 (2024): 173397. https://doi.org/10.1016/j.jallcom.2023.173397

[S9] Yang T, Li Q, Liu Z, et al. "Stabilizing the deep sodiation process in layered sodium manganese cathodes by anchoring boron ions." *Advanced Materials* 36.17 (2024): 2306533. https://doi.org/10.1002/adma.202306533

[S10] Cheng C, Ding M, Yan T, et al. "Anionic redox activities boosted by aluminum doping in layered sodium-ion battery electrode." *Small Methods* 6.3 (2022): 2101524. https://doi.org/10.1002/smtd.202101524

[S11] Li Z, Kong W, Yu Y, et al. "Tuning bulk O2 and nonbonding oxygen state for reversible anionic redox chemistry in P2-layered cathodes." *Angewandte Chemie* 134.16 (2022): e202115552. https://doi.org/10.1002/ange.202115552

[S12] Voronina N, Shin M Y, Kim H J, et al. "Hysteresis-suppressed reversible oxygen-redox cathodes for sodium-ion batteries." *Advanced energy materials* 12.21 (2022): 2103939. https://doi.org/10.1002/aenm.202103939

[S13] Hwang J Y, Kim J, Yu T Y, et al. "A new P2-type layered oxide cathode with extremely high energy density for sodium-ion batteries." *Advanced Energy Materials* 9.15 (2019): 1803346. https://doi.org/10.1002/aenm.201803346

[S14] Liu S, Wan J, Ou M, et al. "Regulating Na occupation in P2-type layered oxide cathode for all-climate sodium-ion batteries." *Advanced Energy Materials* 13.11 (2023): 2203521. https://doi.org/10.1002/aenm.202203521

[S15] Yang L, Li X, Liu J, et al. "Lithium-doping stabilized high-performance P2–$Na_{0.66}Li_{0.18}Fe_{0.12}Mn_{0.7}O_2$ cathode for sodium ion batteries." *Journal of the American Chemical Society* 141.16 (2019): 6680-6689. https://doi.org/10.1021/jacs.9b01855

[S16] Chen D, He B, Jiang S, et al. "Enhancing the structural stability and strength of P2-type layered oxide sodium ion battery cathodes by Zn/F dual-site doping." *Chemical Engineering Journal* 510 (2025): 161676. https://doi.org/10.1016/j.cej.2025.161676

[S17] Li H, Liu M, Shi J, et al. "Green and low-cost modified $Na_4Fe_3(PO_4)_2(P_2O_7)$ cathode material for sodium-ion batteries with wide temperature operation." Journal of Alloys and Compounds (2026): 185967. https://doi.org/10.1016/j.jallcom.2026.185967

[S18] Zeng J, Gao J, Jian W, et al. "Multivalent Cation Incorporated into Manganese-Iron Based NASICON Cathodes for High Voltage Sodium-Ion Batteries." Advanced Functional Materials 34.52 (2024): 2410992. https://doi.org/10.1002/adfm.202410992

[S19] Liu Y, Rong X, Bai R, et al. "Identifying the intrinsic anti-site defect in manganese-rich NASICON-type cathodes." *Nature Energy* 8.10 (2023): 1088-1096. https://doi.org/10.1038/s41560-023-01301-z

[S20] Javed O, Mehek R, Ali G, et al. "Equimolar bimetallic vanadium titanium based Prussian blue analogue as zero strain cathode for sodium ion batteries." *Journal of Electroanalytical Chemistry* (2025): 119775. https://doi.org/10.1016/j.jelechem.2025.119775

[S21] Yan X, Yang Y, Liu E, et al. "Improved cycling performance of prussian blue cathode for sodium ion batteries by controlling operation voltage range." *Electrochimica Acta* 225 (2017): 235-242. https://doi.org/10.1016/j.electacta.2016.12.121

[S22] Zhong J, Xia L, Chen S, et al. "Coordination engineering for iron-based hexacyanoferrate as a high-stability cathode for sodium-ion batteries." *Proceedings of the National Academy of Sciences* 121.31 (2024): e2319193121. https://doi.org/10.1073/pnas.2319193121

[S23] Shen C, Long H, Wang G, et al. "$Na_3V_2(PO_4)_2F_3$@C dispersed within carbon nanotube frameworks as a high tap density cathode for high-performance sodium-ion batteries." *Journal of Materials Chemistry A* 6.14 (2018): 6007-6014. https://doi.org/10.1039/C8TA00990B

[S24] Fan S, Gao Y, Liu Y, et al. "Recrystallization-driven quasi-spherical Prussian blue analogs with high tap density and crystallinity for sodium-ion batteries." *ACS Energy Letters* 10.4 (2025): 1751-1761. https://doi.org/10.1021/acsenergylett.5c00080

[S25] He S, Shen X, Han M, et al. "High-Voltage $Na_{0.76}Ni_{0.25-x/2}Mg_{x/2}Mn_{0.75}O_{2-x}F_x$ Cathode Improved by One-Step In Situ MgF2 Doping with Superior Low-Temperature Performance and Extra-Stable Air Stability." *ACS nano* 18.17 (2024): 11375-11388. https://doi.org/10.1021/acsnano.4c01263

[S26] Liu S, Wan J, Ou M, et al. "Regulating Na occupation in P2-type layered oxide cathode for all-climate sodium-ion batteries." *Advanced Energy Materials* 13.11 (2023): 2203521. https://doi.org/10.1002/aenm.202203521

[S27] Peng B, Zhou Z, Xu J, et al. "Crystal facet design in layered oxide cathode enables low-temperature sodium-ion batteries." *ACS Materials Letters* 5.8 (2023): 2233-2242. https://doi.org/10.1021/acsmaterialslett.3c00625

[S28] Yang C, Liu X, Lin Y, et al. "Entropy-driven solvation toward low-temperature sodium-ion batteries with temperature-adaptive feature." *Advanced Materials* 35.28 (2023): 2301817. https://doi.org/10.1002/adma.202301817

[S29] Li Y, Zhao Y, Feng X, et al. "A durable P2-type layered oxide cathode with superior low-temperature performance for sodium-ion batteries." *Science China Materials* 65.2 (2022): 328-336. https://doi.org/10.1007/s40843-021-1742-8